Three-Dimensional Parameterization of Submesoscale Eddy From HiSea-II Imagery

Linyao Ge, Ge Chen, *Senior Member, IEEE*, Daosheng Wang, Xiaoyan Chen, Zhongping Lee, *Member, IEEE*, and Baoxiang Huang, *Senior Member, IEEE*

***Abstract*—The detection of submesoscale eddies is limited by altimeter resolution and the complex dynamics of eddy formation and dissipation, resulting in an incomplete understanding of their structure. The advent of multiband high-resolution satellites, such as HiSea-II, enables more detailed observations of submesoscale eddies. This study presents a comprehensive methodology for parameterizing eddy properties. We model eddy morphology using a logarithmic spiral expression and employ deep learning and partial differential equations to extract streamlines representing the static transport state. The spiral is then fitted to parameterize attributes such as core location, radius, and polarity. Furthermore, a three-dimensional logarithmic spiral is introduced to characterize the eddy vertical extent. Analysis of 21 submesoscale eddies in 9 HiSea-II images demonstrates that our proposed method surpasses an existing deep-learning model in accuracy by about 70% for the eddy core position. Validation using reanalysis ocean current data and high-resolution Chlorophyll-a concentration data confirms that these eddies have a radius of 3.7 $\pm$ 2.5 km and a mean depth of 42 m. This approach overcomes the limitations of altimeter-based eddy observations in nearshore regions, provides a novel and precise parameterization of submesoscale eddies in optical imagery, and enhances the utility of multiband high-resolution SmallSats such as HiSea-II.**

***Index Terms*—Chan-Vese model, convolution neural network, HiSea-II SmallSat, logarithmic spiral, parameterization, submesoscale eddy.**

Received 13 December 2024; revised 11 March 2025 and 17 May 2025; accepted 24 July 2025. Date of publication 28 July 2025; date of current version 27 August 2025. This work was supported in part by the National Natural Science Foundation of China under Grant 42030406, and in part by the International Research Center of Big Data for Sustainable Development Goals under Grant CBAS2022GSP01. *(Corresponding authors: Zhongping Lee; Baoxiang Huang.)*

Linyao Ge and Xiaoyan Chen are with the State Key Laboratory of Physical Oceanography, Ocean University of China, Qingdao 266100, China (e-mail: linyaoge@stu.ouc.edu.cn; xiaoyanchen@ouc.edu.cn).

Ge Chen is with the State Key Laboratory of Physical Oceanography, Department of Marine Technology, Ocean University of China, Qingdao 266100, China, and also with the Laboratory for Regional Oceanography and Numerical Modeling, Laoshan Laboratory, Qingdao 266100, China (e-mail: gechen@ouc.edu.cn).

Daosheng Wang and Zhongping Lee are with the State Key Laboratory of Marine Environmental Science College of Ocean and Earth Sciences, Xiamen University, Xiamen 361005, China (e-mail: dswang@xmu.edu.cn; zpli2015@xmu.edu.cn).

Baoxiang Huang is with the College of Computer Science and Technology, Qingdao University, Qingdao 266071, China, and also with the Laboratory for Regional Oceanography and Numerical Modeling, Qingdao Marine Science and Technology Center, Qingdao 266100, China (e-mail: baoxianghuang@qdu.edu.cn).

This article has supplementary downloadable material available at https://doi.org/10.1109/JSTARS.2025.3593267, provided by the authors.

Digital Object Identifier 10.1109/JSTARS.2025.3593267

I. Introduction

OCEANIC eddy, analogous to storms in atmospheric space, is an essential phenomenon that affects energy [1], climate [2], [3], and has profound impacts on energy transport, substance entrainment, and ecosystem dynamics [4], [5]. Advances in satellite observations and extensive studies of oceanic eddies have contributed to a better understanding of the morphology, dynamics, and ecology of mesoscale eddies. The submesoscale eddy is a pivotal phase in the oceanic eddy life cycle whose diameter is less than Rossby's radius of deformation and scale ranges approximately 0.1–10 km in horizontal [6], and 0.01–1 km in vertical scales [7], [8]. The geographical distribution of these eddies, as observed through optical methods, is primarily near the coast [9]. They exhibit distinct characteristics of unsteady states and nongeostrophic motion. These eddies play significant roles in the transport of materials offshore and contribute to various dynamical processes such as the front and upwelling [10], [11], [12], [13].

In contrast to submesoscale eddies, current research has extensively explored mesoscale eddies in the ocean. These eddies can be identified and their trajectories can be predicted through deep learning models [14], [15], and their three-dimensional structures and vertical profiles can be examined using in-situ observational data, such as that obtained from many Argos [16], [17], [18]. The global oceanic eddy studies typically rely on the identification and tracking data derived from grid products generated using altimeter measurements [19], [20], to analyze the morphology and dynamics of mesoscale eddies by their parameters such as core position, radius, and amplitude. However, the spatial resolution of these grid products is insufficient to capture the more abundant submesoscale eddies, resulting in a large underestimation of the density of eddies, where only between 6% and 16% of the total number of eddies reported [21]. Therefore, it is crucial to identify and parameterize these unobserved eddies by integrating additional satellite datasets alongside various observational methodologies. In diverse oceanic regions, researchers have employed a combination of model simulations [22], [23], [24] and other data sources, such as HF radar data [25], [26], drifter records, and glider observations to explore oceanic eddies [27]. In recent years, many studies have been carried out to characterize the topology structure of submesoscale eddies, which include using high-resolution simulation data [28], [29], [30], ocean color (chlorophyll) data [31], and reanalysis dataset [32].

Due to the transient nature of submesoscale eddies [33], high-resolution oceanic data is crucial for exploring their characterization. Consequently, the $1/100^\circ$ HYCOM model [34] and $1/48^\circ$ ECCO estimates [35] are employed to quantify the number of submesoscale eddies and to extract their structural characteristics. These high-resolution simulations and reanalysis datasets are computed based on oceanic and climatological physical models, which can exhibit biases compared to the actual marine environment [36]. Moreover, the introduction of new ocean color satellite products and enhanced algorithms have effectively addressed the challenges associated with observing submesoscale eddies [33]. Different measurement systems, such as synthetic aperture radar (SAR) [37], high-frequency radar (HFR) systems, and long-term arrays of satellite optical measurements, have been used to detect submesoscale eddies [38], [39]. Although numerous researchers have utilized various high-resolution datasets to identify submesoscale eddies [40], [41], [42], estimate their properties, and analyze their numbers and impacts, there remains a scarcity of studies focused on detecting and estimating the parameters of submesoscale eddies using high-resolution watercolor imagery ($<$100 m) captured by satellites.

The observation of submesoscale eddies requires high-resolution and highly sensitive satellite measurements. The HiSea-II satellite operated by Xiamen University, China, is a multiband SmallSat aimed at the ecosystems of coastal marine environments [43]. It has 6 narrow bands in the visible domain, along with a 20 m spatial resolution and $\sim$270 signal-to-noise ratio, making it effective in capturing fine-scale variation of phytoplankton (change of watercolor) in the coastal environment. Such changes in biology reflect the dynamic nature of coastal environments, which include the processes of currents and submesoscale eddies. Compared numerous studies using optical satellites such as SDGSAT-1 [9], [40] and GOCI-I [44], SAR such as Sentinel-1 [45], [46], infrared satellites [47], and altimeters like SWOT [48] for exploring submesoscale eddy, HiSeaII, a 65-kg SmallSat, has high spatial resolution and SNR, which offer a distinct advantage in observing submesoscale phenomena. The utilization of HiSea-II for observing submesoscale eddies not only demonstrates its potential for oceanographic applications but also affirms the capability of small satellites in capturing submesoscale phenomena. Furthermore, this study underscores the growing significance of SmallSats, such as HiSea-II, in addressing challenges in nearshore marine science and advancing the frontiers of ocean observation.

The morphological information of eddies is primarily captured through the identification of gradient changes in watercolor features at their edges and the segmentation of different regions based on watercolor. Therefore, the parameterization of the morphological properties of submesoscale eddies can be transformed into a scheme in image processing. Deep learning methods [49], [50] are currently the most popular approaches for this task such as object edge (the gradient changes) detection [51]. Furthermore, deep learning as a data-driven method has a powerful representative learning capacity [52] and is widely used in oceanography [53], [54], [55], geoscience [56], [57], and climatology [58], [59].

However, the utilization of a deep learning approach for segmenting regions requires a significant amount of labeled data, which is currently unavailable for HiSea-II. Model-driven methods, which are based on modeling partial differential equations, offer advantages such as not requiring large training datasets, improved interpretability, and better performance compared to data-driven approaches. Among them, the Chan-Vese model [60] is a popular method with good performance for image vision and high-dimensional data classification [61]. Therefore, HiSea-II images can be used to segment different watercolor regions that are influenced by the entrainment effect of submesoscale eddies.

Regarding morphological characteristics, the core and scale of the eddy are crucial parameters. For mesoscale eddy, based on the grided production of absolute dynamic topography, sea level anomaly, and geostrophic flow, [62] used the center of the best-fitting velocity circle as the eddy core position, while Tian et al. [20] used the center of the innermost contour as the eddy core. Although these methods are valuable for calculating parameters such as eddy core, energy, and amplitude, it is important to note that the closed forms of eddies are not obtained based on the watercolor features observed in the HiSea-II images. Meanwhile, the shape of the submesoscale eddy is nonlinear which is similar to "cat-eye" [63] and is difficult to describe with mathematics. To calculate the location and scale of the submesoscale eddy as accurately as possible, we transform the submesoscale nonlinear shape into a linear logarithmic spiral shape. It can approximate the static rotational patterns resulting from the diffusion of matter due to the eddy's wrapping effect. Furthermore, we employ a robust regression method to fit the logarithmic spirals and then estimate the optimal core and radius of the submesoscale eddies. In order to evaluate model performance, we adopted mean absolute error (MAE) and the mean geodetic distance (MGD) to compute the error of the estimated eddy core. In addition, we match the estimated parameters with other data, such as chlorophyll-a (Chl-a) concentration and high-resolution ocean current, to verify the rationality and authenticity of the results derived from our methodology. The main contributions can be summarized as follows.

1) HiSea-II, a SmallSat capable of capturing fine-resolution images at multiple visible wavelengths, was first adopted to observe submesoscale eddies based on their optical characteristics.
2) A novel parameterization framework for submesoscale eddies is designed, integrating neural networks with partial differential equations to extract different optical features of these eddies.
3) Based on the features extracted by the neural network and partial differential equations, we employed the logarithmic spiral to describe the streamlines of submesoscale eddies and calculate their core positions and radii.
4) We used marine data to verify the parameterization results. The experiment demonstrates that the estimated parameters from our proposed framework are reasonable.

The rest of this article is organized as follows. Section II describes the HiSea-II image data, ocean remote sensing data, and computer vision data. Section III presents the proposed

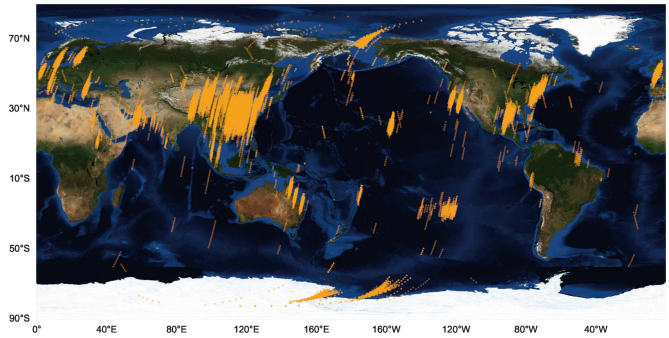

Fig. 1. HiSea-II data distribution as of 2 June 2023.

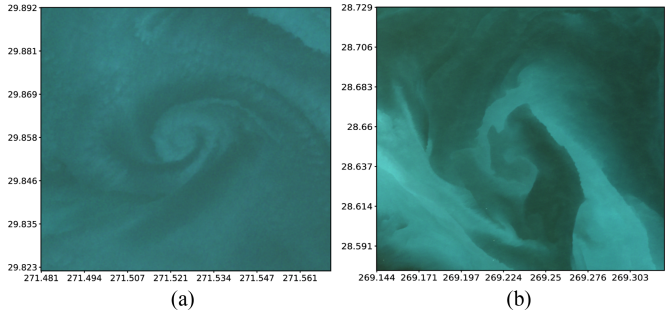

Fig. 2. Primary features of submesoscale eddy morphology observed in HiSea-II images. False-color is only used to enhance the visualizations. (a) "Thread" feature. (b) "Ribbon" feature.

methodology. Section IV presents the extensive experiment and related analysis are presented. Finally, Section V concludes this article.

II. Dataset

A. HiSea-II Data

HiSea-II was launched on 11 June 2021, which, as depicted in Fig. 1, has captured nearly thirty thousand images worldwide so far. HiSea-II has 8 bands covering the visible to near-infrared domain, with the center wavelengths as 450, 490, 570, 625, 680, 710, 745, and 865 nm, respectively. The visible spectrum, with 20 m spatial resolution and ~ 270 signal-to-noise ratio, is effective in capturing the fine structures of the coastal marine environment. For the development and evaluation of the proposed method for submesoscale identification and characterization, we selected 20 images where offshore eddies are present and chose 9 best-quality images for manual detection of submesoscale eddies. These images were taken in the Black Sea, the East China Sea, the Gulf of Mexico, and the English Channel. For these images, pseudotrue-color images were produced with the first three bands as blue, green, and red, respectively.

B. Marine Data

1) Chl-a Data: We validated the submesoscale eddies by comparing them with the Chl-a datasets from the GOCI-II and GCOM-C satellites. The GOCI-II satellite offers a spatial resolution of 250 m with a temporal resolution of one hour. This marks an improvement in spatial resolution compared to its predecessor, GOCI-I. Consequently, we utilized both Chl-a data from GOCI-II and GCOM-C to validate the submesoscale eddies in the East China Sea as captured by HiSea-II. For submesoscale eddies in other research regions, we employed Chl-a concentration data from the JAXA GCOM-C satellite with the 250 m resolution.

2) Ocean Current Data: The parameterized depth of submesoscale eddies must remain within the bounds of the actual water depth. Consequently, we employed the ETOPO 2022 global relief model, which seamlessly integrates topographic and bathymetric data at a 15-arc-second resolution [64] to conduct a preliminary verification of the depth estimation results. Subsequently, we utilized the HYCOM-TSIS $1/100^\circ$ Gulf of Mexico reanalysis current data available at: https://www.hycom.org/data/gomb0pt01/gom-reanalysis. This dataset is boxcar-averaged to remove small-scale variability, enabling the observation of submesoscale phenomena and depth verification.

C. Computer Vision Data

Pattern analysis, statistical modeling, and computational learning (PASCAL) VOC 2012 and BSDS500, two well-established public datasets, were employed to train and fine-tune the proposed neural networks, respectively.

PASCAL VOC 2012, as described in [65], is the dataset utilized in The PASCAL visual object classes challenge 2012. This dataset has earned recognition as a benchmark dataset for tasks related to object classification, recognition, segmentation, and detection. The dataset comprises 5011 images for training and 4952 images for testing, encompassing 20 different categories of objects and scenes, spanning a wide range of complex scenes, such as individuals, vehicles, animals, and more. The dataset is available at: http://host.robots.ox.ac.uk/pascal/VOC/voc2012/ (The PASCAL Visual Object Classes Challenge 2012).

BSDS500, in [66], is a dataset made available by the Computer Vision Group at the University of California, Berkeley, and is primarily employed for image segmentation and object edge detection tasks. This dataset is composed of 200 training images, 100 validation images, and 200 testing images, sourced from diverse scenes, including natural landscapes, cityscapes, and interior environments. The dataset can be accessed at: https://www2.eecs.berkeley.edu/Research/Projects/CS/vision/bsds/ (The Berkeley Segmentation Dataset and Benchmark).

III. Methodology

A. Overall Architecture

Accurate determination of the core position, scale, and vertical depth of submesoscale eddies from optical images requires careful consideration of the complex ocean environment. To address this, we categorize the subimages based on the two main watercolor features, "Thread" and "Ribbon" such as Fig. 2(a) and (b), presented by eddies in HiSea-II images that predominantly contain submesoscale eddies into two groups. We then develop two branches to extract the streamline of submesoscale eddies from these subimage categories. To estimate the parameters, including the core position and radius of the

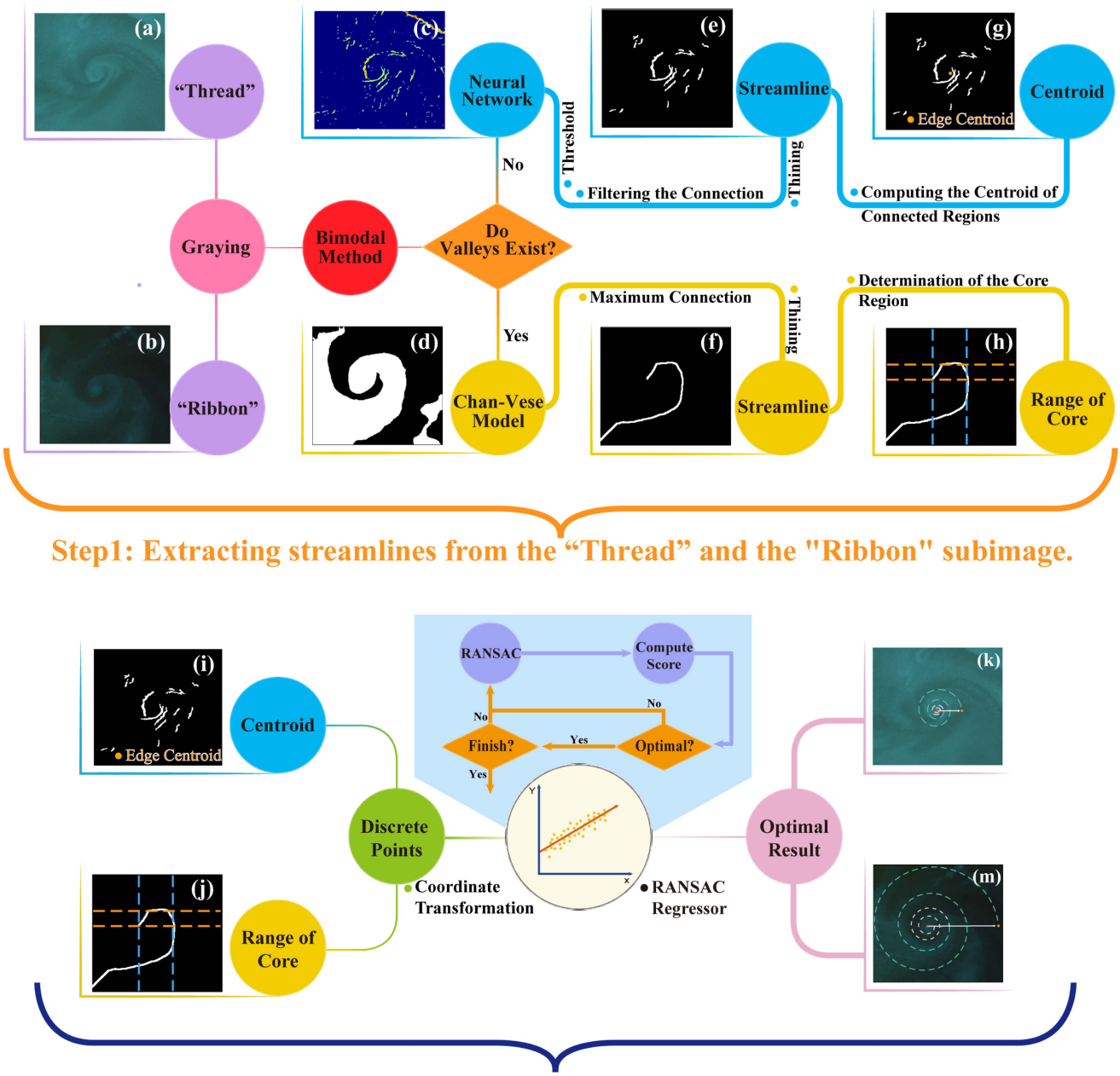

Fig. 3. Pipeline of estimating the parameters of submesoscale eddy using HiSea-II image. All the false-color images are only used to enhance the visualizations.

submesoscale eddies, we employ a robust regression algorithm that fits logarithmic spirals. Moreover, we introduce the concept of a three-dimensional spiral to estimate the vertical extension of the eddies. The complete parameterization method is visually illustrated in Fig. 3, providing a comprehensive overview of our approach.

B. "Thread" and "Ribbon" Characteristics

The morphology of eddies can undergo significant changes depending on their developmental stage. In the submesoscale eddies captured in HiSea-II images, these variations are primarily reflected in their watercolor characteristics. Despite the intricate influences of these eddies for watercolor, two primary types of features are observed in submesoscale eddies from HiSea-II images.

The first feature involves active eddies located in regions with high concentrations of nutrients and tracers. These eddies bring about alterations in the vertical distribution of these substances due to convergence and dispersion effects induced by the eddies. This leads to alternating bright and dark patterns in the water coloration within the eddy, resulting in a distinctive watercolor profile inside the eddy. An illustrative example of this feature can be seen in Figs. 2(a) and 3(a).

The second key feature is observed when the eddy moves into a low-concentration zone or the interface between high and low-concentration regions. In such situations, the eddy induces the dispersion of substances from areas of high concentration to

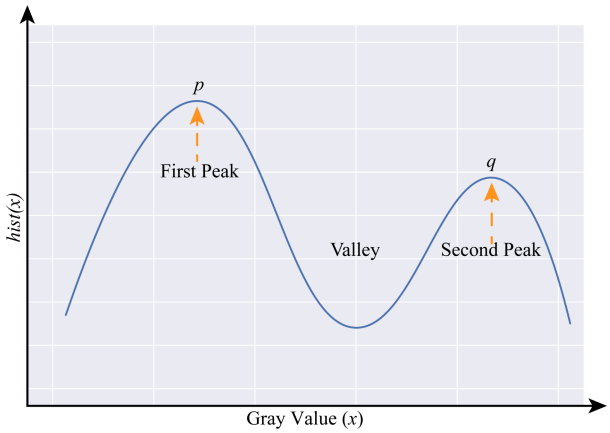

Fig. 4. Schematic diagram for two peaks and the valley in the bimodal method.

areas of lower concentration, primarily through the entrainment effect exerted by the eddy on these substances. This process creates a noticeable "pulling" effect within the water color, as demonstrated in Figs. 2(b) and 3(b).

These distinct characteristics have guided us in developing appropriate models for a more precise parameterization of submesoscale eddies. To facilitate differentiation, we have chosen the terms "Thread" and "Ribbon" to subjectively describe these two distinctive features.

In order to categorize HiSea-II submesoscale eddy images based on these features in an adaptive manner, we adopted a bimodal method, which is an image processing method for segmenting foreground and background. First, for each eddy patch, we chose the three spectral bands of the HiSea-II image to generate pseudocolor images and converted them into grayscale to compute the grayscale histograms. According to that, the gray level that appears most time in each image can be obtained, which can be regarded as the first peak that is denoted p. Then, the second peak q is calculated via the following function:

$$q = \text{argmax}((x-p)^2 * \text{hist}(x)) \tag{1}$$

where x is the gray value of pixels of the patch, whose range is $[0, 255]$. $\text{hist}(x)$ in (1) is the gray level histogram computed by x. Between these peaks, there is a minimum value which is all less than the peak value. This characteristic results in the fitted curve based on the histogram exhibiting a distinct "valley" shape, as illustrated in Fig. 4. Based on the value of this valley, the branches of "Thread" and "Ribbon" can be effectively distinguished to implement targeted parameterization.

C. Streamline in "Thread"

Based on the analysis of these patches, the "Thread" category exhibits significant gradient variations of watercolor near the edge of the rotating fluid. Therefore, extracting the streamlines in the "Thread" category aims to capture the locations where the gradient changes the most, which can be accomplished by employing edge detection methods. In computer vision, this is a classical problem and there are many models with excellent performance, such as the typical Sobel operator and the creative transformer model. Given the complexity of this task, as well as the model's performance and parameter count, we developed a neural network based on the U-Net [67] architecture, a type of fully convolutional neural network [49], which outperforms classical detection methods [68]. The U-Net model is primarily focused on medical image detection tasks, such as vascular [69] and road information [70]. The characteristics of streamline detection are similar to the aforementioned task, particularly in terms of the imbalance between edges and background, as well as the limited amount of training data. Therefore, for streamline extraction, the constructed model further reduced the parameters of the neural network, with the network's structure schematically depicted in Fig. 5. This neural network adopted an encoder–decoder structure. Due to the scarcity of labeled HiSea-II images for training and the lack of eddy label information, we employed transfer learning. We initially trained the network on the VOC dataset, followed by fine-tuning the decoder using the specialized edge-detection BSDS dataset. Concurrently, all data were converted into grayscale images to standardize the probability distributions of eigenvalues across real and pseudocolor image samples. These grayscale images were then input into the neural network. First, the data passes through the encoder, which extracts texture and deep semantic features. These extracted features are then transferred to the decoder. In the decoder, an upsampling process is employed to gradually convert features into final detection results. Meanwhile, the model employs short connection operations in the decoder to combine semantic and texture features, thereby enhancing detection accuracy. The neural network's training process is guided by the loss function described in the following equation:

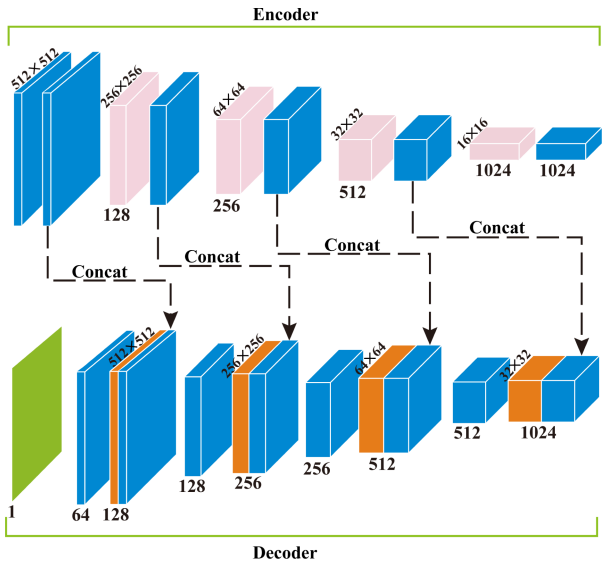

Fig. 5. Structure of the fully convolutional neural networks for transfer learning.

$$\mathcal{L} = \frac{1}{n}\sum_{i=1}^{n} -w_n[y_n \cdot \log\sigma(x_n) + (1-y_n)\cdot\log(1-\sigma(x_n))]. \tag{2}$$

This loss function integrates the sigmoid activation with binary cross-entropy loss, allowing for class weighting to mitigate

sample imbalance. The output of the neural network is shown in Fig. 3(c). Nevertheless, it is expected that noisy information will still be present in the processed HiSea-II images, which can also be detected by the neural network. To prevent this noise from affecting the subsequent fitting process, the output φ of the neural network is mapped using a threshold k, which can be adjusted based on the size of the detected edge. This threshold is formalized by an equation as follows:

$$\varphi(\mathbb{P}) = \begin{cases} 1 & \mathbb{P} \geq k \\ 0 & \text{otherwise} \end{cases} \tag{3}$$

where $\mathbb{P}$ is the result of the last layer of neural network features after calculation by softmax function. Then, depending on the number of pixels contained in the connected domain, the noise portion can be removed. Next, we adopted a thinning model [71] to extract the main information of every connected domain as displayed in Fig. 3(e). Based on these points, the centroid point ξ can be computed, and the range of core of the eddy located can be confirmed as $e_m \in [\xi_m - \delta, \xi_m + \delta]$, $e_n \in [\xi_n - \delta, \xi_n + \delta]$, where δ is a relaxed value used to expand or narrow a search, e is the index of points in range of core of eddy, m is the horizontal axis, and n is the vertical axis. The final result of the neural network channel is shown in Fig. 3(g).

D. Streamline in "Ribbon"

Compared with the "Thread," the "Ribbon" has a distinct difference in watercolor between foreground and background. According to this characteristic, the watercolor bands pulled out by the entrainment effect of the eddy can be segmented. Deep learning methods have strong performance for image semantic segmentation, however, the data size does not support the training. Thus, we adopt the Chan-Vese model to segment the zone of the eddy, which is a model-driven method with strong image segmentation performance and interpretability that is more suitable for this task. The energy function of the Chan-Vese model is described as follows:

$$\begin{aligned} E(c_1, c_2, u) = \gamma & \int_\Omega |\nabla u(x)| dx \\ & + \alpha_1 \int_\Omega (f(x) - c_1)^2 u(x) dx \\ & + \alpha_2 \int_\Omega (f(x) - c_2)^2 (1 - u(x)) dx, \end{aligned} \tag{4}$$

where α_1, α_2, and γ are the penalty parameters, c is an arbitrary curve, c_1 is the mean gray inside of c, c_2 is outside of c, x denotes the pixels of the image, $u(x)$, $1 - u(x)$, and $f(x)$ are the function of the object, background, and the whole image, respectively. $\int_\Omega |\nabla u(x)| dx$ is the regular term, which is used to retain the smoothness of segmentation. Equation (4) is solved iteratively by setting parameters, updating the $u(x)$, c_1, and c_2, until getting the minimum energy function in limited steps. This process can be formulated as follows:

$$\left(c_1^{k+1}, c_2^{k+1}, u^{k+1}\right) = \underset{c_1, c_2, u \in [0,1]}{\arg\min} \; E\left(c_1^k, c_2^k, u^k\right) \tag{5}$$

where $k \in \mathbb{K}$ is the iteration step, u^{k+1} is the segmentation result at $k+1$ step. However, deriving the derivative for $\int_\Omega |\nabla u(x)| dx$ will produce a Laplace term and the solution process will be extremely complex. Therefore, an iteration method such as the alternating direction method of multipliers is adopted to divide (4) into subproblems. The $\vec{w}$ is introduced instead of ∇u, the (4) can be transformed into the following:

$$\begin{aligned} E(c_1, c_2, u, \vec{w}) = \gamma & \int_\Omega \vec{w} dx \\ & + \alpha_1 \int_\Omega (f(x) - c_1)^2 u(x) dx \\ & + \alpha_2 \int_\Omega (f(x) - c_2)^2 (1 - u(x)) dx \\ & + \int_\Omega \vec{\lambda}^k \cdot (\vec{w} - \nabla u) dx \\ & + \frac{\mu}{2} \int_\Omega |\vec{w} - \nabla u|^2 dx. \end{aligned} \tag{6}$$

Furthermore, c_1, c_2 can be calculated iteratively by

$$c_1^{k+1} = \frac{\int_\Omega f(u^k) dx}{\int_\Omega u^k dx}, c_2^{k+1} = \frac{\int_\Omega f(1 - u^k) dx}{\int_\Omega (1 - u^k) dx} \tag{7}$$

where k is the step. $u(x)$ can be computed by the following:

$$\begin{aligned} u(x)^{k+1} = & \int_\Omega \alpha_1 (f - c_1^{k+1})^2 - \alpha_2 (f - c_2^{k+1})^2 dx \\ & + \frac{\mu}{2} \int_\Omega |\vec{w} - \nabla u + \frac{\lambda^k}{\mu}|^2 dx. \end{aligned} \tag{8}$$

Then, the $\vec{w}$ can be updated by the soft threshold

$$\vec{w}^{k+1} = \max\left(|\nabla u^{k+1} - \frac{\lambda^k}{\mu}| - \frac{\lambda}{\mu}, 0\right) \frac{\nabla u^{k+1} - \frac{\lambda^k}{\mu}}{|\nabla u^{k+1} - \frac{\lambda^k}{\mu}|}. \tag{9}$$

Finally, the Lagrange multiplier can be iterated by

$$\lambda^{k+1} = \lambda^k + \mu(\vec{w}^{k+1} - \nabla u^{k+1}). \tag{10}$$

The iterative process is terminated when the condition $\frac{E^{k+1} - E^k}{E^k} \leq \epsilon$ is met, yielding the segmentation results shown in Fig. 3(d).

In order to accurately parameterize the eddy core and minimize the spatial and temporal complexity of the model, we adopt a selection strategy that involves choosing the largest connected domain after deblurring like Fig. 3(f). This selected domain exhibits the characteristic spiral line rotating inward, as depicted in Fig. 3(h). Therefore, it can be regarded as a streamline, from which a spiral curve can be fitted. In the spiral curve, whether Fermat's spiral, Archimedean spiral, or logarithmic spiral, the point of intersection is increased with nearing the origin as displayed in Fig. 6. Hence, the points of the streamline are denoted as $e = \{e_m, e_n\}_{\text{CV}}$, the extent of the core can be determined that is $[\eta_{m_1} : \eta_{m_2}, \eta_{n_1} : \eta_{n_2}]$.

E. Logarithmic Spiral Approximation

Despite oceanic eddies being spirals on the sea, submesoscale eddies adhere to the conservation of the potential vorticity, and

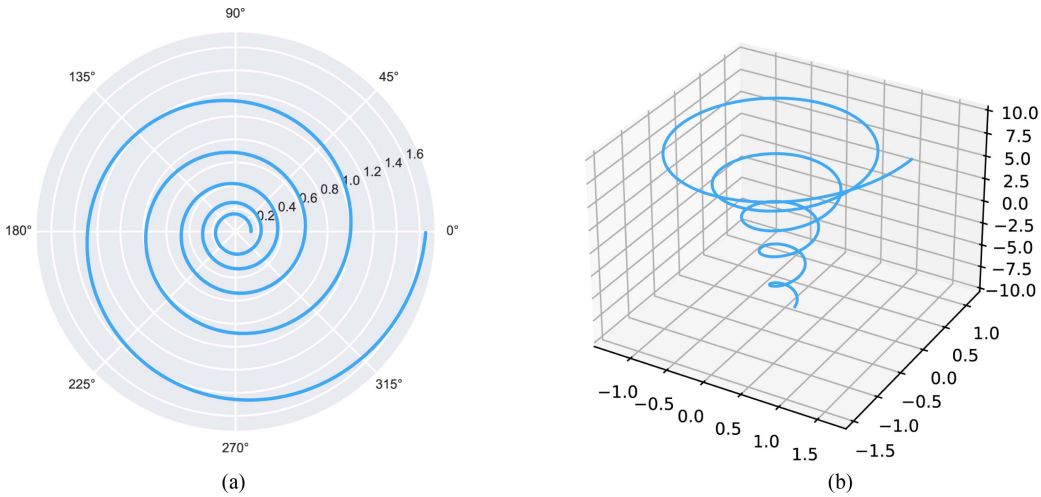

(a) (b)

Fig. 6. Diagram of the logarithmic spiral curve $r = ae^{b\theta}$ with $a = 1, b = 0.08$. (a) Logarithmic spiral. (b) 3-D logarithmic spiral.

their shape has nonlinear features. To simplify the problem, we approximate the shape of the submesoscale eddy to a logarithmic spiral as

$$r = ae^{b\theta} \tag{11}$$

the ideal regular geometry in flat and three-dimensional forms is illustrated in Fig. 6. In the expression, θ and r denote the polar angle and radius, respectively, while the unknown parameters a and b need to be reckoned to confirm the optimal logarithmic spiral. In order to obtain the optimal spiral, first, a point is tentatively designated as the eddy core (c_i, c_j), which is from the following set:

$$\mathbb{D} = \begin{cases} \left\{ (c_i, c_j) \middle| \begin{matrix} c_i & \in [\xi_m - \delta, \xi_m + \delta] \\ c_j & \in [\xi_n - \delta, \xi_n + \delta] \end{matrix} \right\} & \text{for “Thread”} \\ \left\{ (c_i, c_j) \middle| \begin{matrix} c_i & \in [\eta_{m_1}, \eta_{m_2}] \\ c_j & \in [\eta_{n_1}, \eta_{n_2}] \end{matrix} \right\} & \text{for “Ribbon.”} \end{cases} \tag{12}$$

The fitting dataset $\mathbb{D}$ is the features of the streamline extracted by the neural network and the CV model. Due to the logarithmic spiral being a function of polar coordinates, this $\mathbb{D}$ dataset needs to transfer the coordination system from the Cartesian to the polar via the following equations:

$$r = \sqrt{(d_i - c_i)^2 - (d_j - c_j)^2}, \qquad d \in \mathbb{D} \tag{13}$$

$$\theta = \operatorname{arctran}\left(\frac{d_i - c_i}{d_j - c_j}\right), \qquad d_j \neq c_j \tag{14}$$

where d_i, d_j are the row and column index of points. Logarithmic spirals not only conform to the conventional shape of the oceanic eddy but also have the advantage of being transformed into a linear form by taking the logarithm of both sides of the equation. These peculiarities make the spiral fit accurate and efficient via the significant performance of the linear regression algorithm. The linear function is formulated as

$$\ln(r) = b\theta + \ln(a) \quad a > 0, r > 0. \tag{15}$$

Second, we adopted a stronger reckless regression algorithm along with random sample consensus (RANSAC) [72] to fit the above function. RANSAC is an iterative algorithm that can estimate the parameters from datasets with outliers, commonly applied in fields such as computer vision and data mining. Compared with other regression algorithms, it can exclude dissociation points effectively, improving the accuracy of cores and further elevating the similarity between the fitting spiral curve and the form of the submesoscale eddy.

To confirm the optimal parameters and cores of the submesoscale eddies, a scoring system is employed to evaluate the fitted spirals. Since the extracted streamline may not precisely follow a logarithmic spiral, traditional regression scores such as MAE and mean squared error, which compute the distance between the dataset and the spiral curve, are not suitable for determining the optimal logarithmic spiral. Utilizing these scores may result in increased parameter estimation errors. Instead, a different approach is taken: the number of intersections between the data points and the curve is counted, and the maximum number of intersections is considered the optimal solution. Its origin represents the optimal core of the submesoscale eddy. Upon analyzing the watercolor patterns in submesoscale eddies in the HiSea-II images and the streamlines we extracted, we observed that these eddies demonstrate a rotation period of one to two weeks. Consequently, we computed the distance between the endpoint of the spiral after completing a 720° rotation and the eddy core to determine the radius of the submesoscale eddy. The horizontal parameters of the submesoscale eddies are obtained, as shown in Fig. 3(k) and (m).

At the vertical dimension, due to the nature of the rotational fluid motion, the radius of an eddy decreases with increasing depth. The depth of the eddy is determined by several factors, including the surface radius, angular velocity, fluid density,

TABLE I
ERROR OF PARAMETERIZED CORE LOCATION IN THE WHOLE AND EVERY REGION

Region	Number	MAE (°)		MGD (km)	
		Our	MEDNet	Our	MEDNet
Total	21	**0.005±0.004**	0.015±0.004	**0.711±0.532**	2.386±0.569
Black Sea	1	**0.009**	0.013	**1.208**	1.759
English Channel	1	**0.014**	0.020	**1.760**	3.7621
East China Sea	8	**0.006±0.004**	0.018±0.003	**0.952±0.567**	2.672±0.386
Gulf of Mexico	11	**0.002±0.001**	0.014±0.003	**0.396±0.205**	2.175±0.367

The bold values indicate the better performance metrics between our proposed method and MEDNet.

and water pressure. However, optical images can only capture the transient state of submesoscale eddy and do not provide information on continuous dynamic parameters. Therefore, in this article, the depth of the eddy's rotation is estimated based on the logarithmic spiral. Initially, we parameterized the surface radius of the eddies. However, it is well-known that the radius of the eddy diminishes with increasing depth. Consequently, the problem involves defining the relationship depth $= f(\text{radius}, \alpha_{\text{radius}})$, where α_{radius} is the rate of decay of radius with depth. Referring to (11), we observe that the r is directly proportional to the θ, which enables the estimation of depth from r by calculating the depth from θ. We convert the dependent and independent variable of (15), which can be derived by collapsing it into

$$\theta = \frac{(\ln(r) - \ln(a))}{b}. \tag{16}$$

When calculating the limit of (11), it is expressed as

$$\lim_{\theta \to -\infty} ae^{b\theta} \to 0, \quad r \to 0. \tag{17}$$

However, when estimating the depth of submesoscale eddies, it is impractical to set $\theta = -\infty$. Therefore, a minimum value of approximately 10^{-32} is assigned to θ, which brings r close to 0. The number of degrees required for the submesoscale eddy to rotate to the bottom in polar coordinates can be determined. This value is then divided by the angular velocity ω of the eddy to calculate the time required for it to reach the bottom.

To determine angular velocity, the planetary vorticity is first calculated using $f = 2\Omega \sin(\varphi)$, where Ω represents the Earth's angular velocity, and φ denotes the latitude. The vorticity of ocean currents relative to the Earth is then computed using the following equation:

$$\xi = \nabla_z V = \frac{\partial v}{\partial x} - \frac{\partial u}{\partial y}. \tag{18}$$

Here, V is the flow velocity vector, with u and v representing the eastward and northward components of the flow velocity, respectively. From ξ and f, the Rossby number $\text{Ro} = \xi / f$ is derived, representing the relative vorticity normalized by planetary vorticity. Subsequently, using Ro as the average vorticity ψ of the eddy, the angular velocity ω can be determined based on Stokes's theorem, as outlined in (19)

$$\psi \times S = \oint_C u \cdot \mathbf{d}l = 2 \times \omega \times S. \tag{19}$$

The rotation time from top to bottom can be calculated using θ/ω, where θ is the angle of rotation and ω is the angular velocity. The depth of submesoscale eddies can be estimated based on ocean current data. We examined the currently available vertical current data, which is accessible only up to 2018. However, due to the small interannual variation and generally low vertical flow velocity, approximately $(1 \sim 50)^{-5}$ cm/s, and the lack of vertical ocean current data after 2021, we adopted the HYCOM hourly data for horizontal current velocity to estimate the depth of submesoscale eddies, taking the lower bound of the final result.

Finally, combined with (16) and (19), the depth of submesoscale eddies can be parameterized by

$$\text{depth} = \lfloor \frac{(\ln(r)) - \ln(a))}{\omega b} \times \sqrt{u^2 + v^2} \rfloor. \tag{20}$$

IV. RESULTS

A. Implementation

1) Neural Network Channel: We initially trained the encoder and decoder using the VOC dataset and then fine-tuned the decoder's parameter gradients using the BSDS dataset to enhance edge detection performance. The encoder consists of four blocks, each comprising a 3×3 convolution layer, batch normalization layer, and max pooling layer. Similarly, the decoder employs four blocks for upsampling using convolution transpose in place of max pooling, followed by a block and a 1×1 convolution kernel for dimension transformation. For training, we set the learning rate as 0.001 and performed 50 epochs on the VOC dataset and 100 epochs on the BSDS dataset. The batch size was set to 4. We employed the RMSprop and Adam optimizers [73] to optimize neural network training on the VOC and BSDS datasets, respectively.

2) Comparative Methods: To verify the performance of our proposed method for estimating the coordinate of the core of submesoscale eddies, we compared the parameterization results with those from the deep learning model MEDNet [9], which also focuses on optical imagery. This model was originally trained on SDGSAT-1 data. To ensure the consistency of input data, we adapted the model by fine-tuning it with HiSea-II data.

3) Evaluation Indicators: We adopt two kinds of evaluation indicators to quantify the results of the experiments. Those are MAE and mean geodesic distance (MGD) on geography.

MAE: It is a widely recognized evaluation metric for regression tasks in machine learning, commonly employed for the

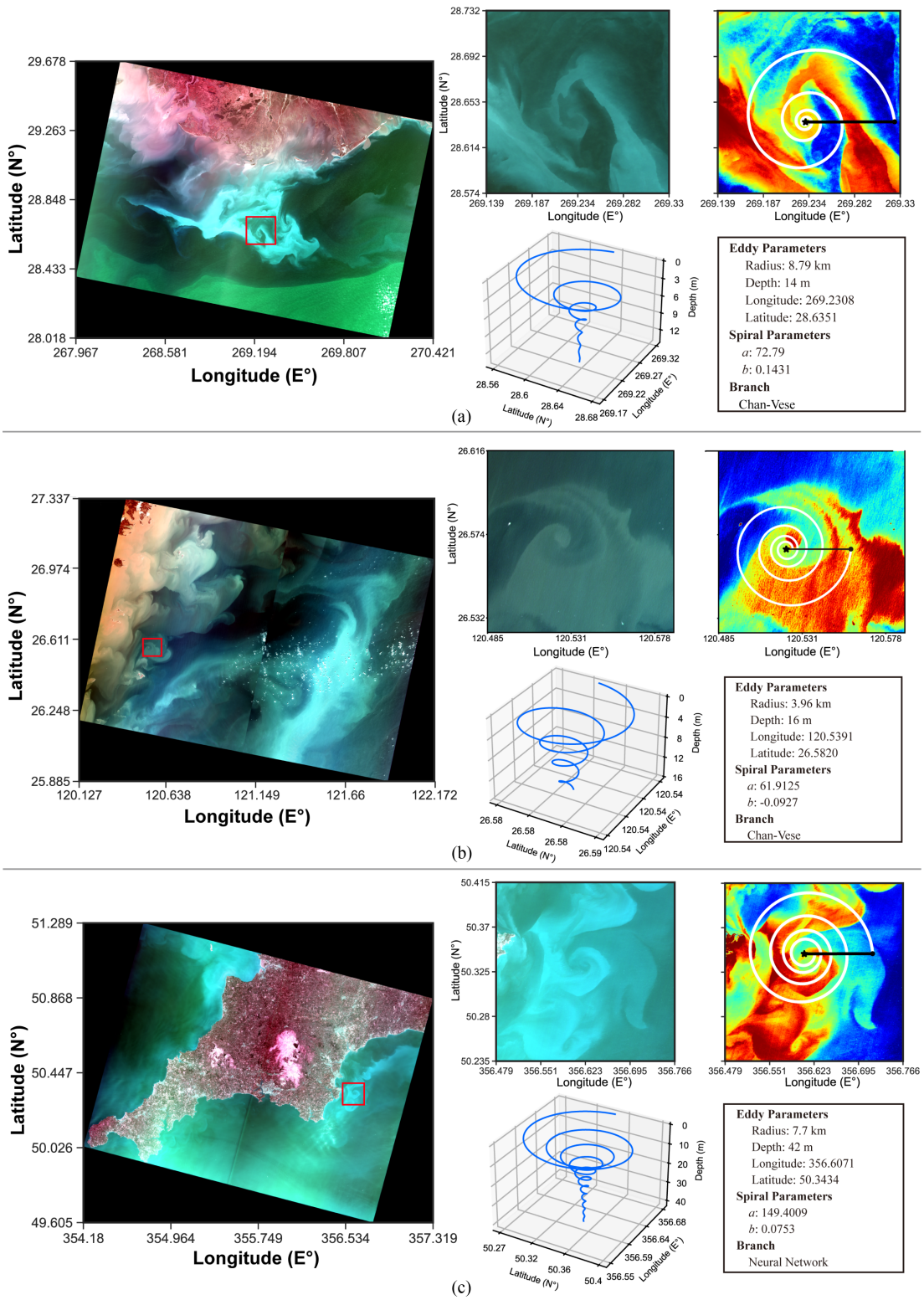

Fig. 7. Part of results of three-dimensional parameterization results for submesoscale eddies. In the false-color subplot, the black pentagram represents the eddy core position and the length of the black line segment is the eddy radius. (a) Imaged on 8 November 2021 at 16:45:16 (UTC) in the Gulf of Mexico. (b) Imaged on 9 April 2023 at 03:02:47 (UTC) in the East China Sea. (c) Imaged on 27 March 2022 at 11:19:16 (UTC) in the English Channel.

quantitative assessment of the discrepancy between predicted values and ground truth. The process for calculating MAE is outlined as follows:

$$\mathrm{MAE} = \frac{1}{n}\sum_{i=1}^{n}|y_i - x_i| \tag{21}$$

where y_i is the prediction results, x_i is the truth, and n is the number of training or testing samples.

MGD: In practical applications, accurate distance calculations must consider the Earth's characteristics. Therefore, we utilize the MGD, which is determined using the great-circle distance formula, as given by

$$\mathrm{MGD} = \frac{1}{n}\sum_{i=1}^{n} r\Delta\hat{\sigma}_i \tag{22}$$

where

$$\Delta\hat{\sigma}_i = 2\arcsin\left(\sqrt{\sin^2\left(\frac{\Delta\phi_i}{2}\right) + \cos\phi_{y_i}\cos\phi_{x_i}\sin^2\left(\frac{\Delta\lambda_i}{2}\right)}\right). \tag{23}$$

In (23), ϕ_y, ϕ_x, λ_y, and λ_x denote the latitude and longitude of the prediction results y_i and the truth x_i, respectively. $\Delta\phi$ and $\Delta\lambda$ are the absolute value of the difference between the ϕ_y, ϕ_x and λ_y, λ_x.

B. Results in Eddy Parameters

The core position, radius, polarity, and depth of 20 submesoscale eddies in 9 HiSea-II images are estimated to demonstrate the effectiveness of the proposed methodology. To enhance the visibility of the submesoscale eddies in the HiSea-II images, we performed image augmentation and adjusted the color coding of the patches to emphasize the variations in watercolor. The spiral fitting results are visualized on these images, and the corresponding parameters including radius, depth, and core position are presented alongside the image. For example, Fig. 7 shows partial results obtained in the Gulf of Mexico, the Black Sea, and the English Channel. The remaining results of these two areas and the results of other regions are included in the supplementary material. In terms of visual perception, the logarithmic spiral fitted by our proposed framework depicts the submesoscale eddy shown in the watercolor image very well. The estimated cores are mostly located at the center of the submesoscale eddies. To quantitatively assess and validate the accuracy of eddy coordinate estimation, we manually labeled the core locations of submesoscale eddies (considered as the "ground truth"). We then calculated the MAE and MGD for the estimated values produced by our proposed framework and by MEDNet, as shown in Table I.

The number following the plus or minus sign in all tables represents the standard deviation, which serves as a measure of the dispersion or variability of the estimated parameters. For parameterizing the core positions of submesoscale eddies, the MAE across all eddies is $0.005 \pm 0.004(^\circ)$, compared to $0.015 \pm 0.004(^\circ)$ for MEDNet. In specific regions, such as the Black Sea and the English Channel, the MAE values are 0.009° and 0.014°, respectively, reflecting an approximate 30% reduction in error compared to MEDNet. The MAE values for the East China Sea and the Gulf of Mexico are $0.006 \pm 0.004(^\circ)$ and $0.002 \pm 0.001(^\circ)$, respectively, indicating accuracy improvements of 60% and 80%. These values demonstrate the robust performance of the proposed framework in parameterizing the core coordinates of submesoscale eddies across different regions. This also confirms that the proposed method for core coordinate estimation is superior to the existing vision-based deep learning model. In practical marine exploration, such as accurately deploying Argo floats and other in situ equipment according to eddy positions, it is crucial to account for physical distance errors on the Earth's surface. Therefore, we calculated the MGD error to analyze discrepancies in a real oceanic environment. Table I shows that the mean great circle distance of our proposed model is less than 1 km. This indicates that most of the estimated submesoscale eddy cores are within the eddies' range. In contrast, MEDNet's MGD exceeds 2 km, approximately 70% higher than our proposed method. This further demonstrates the accuracy and effectiveness of our proposed framework in the 2-D parameterization of submesoscale eddies.

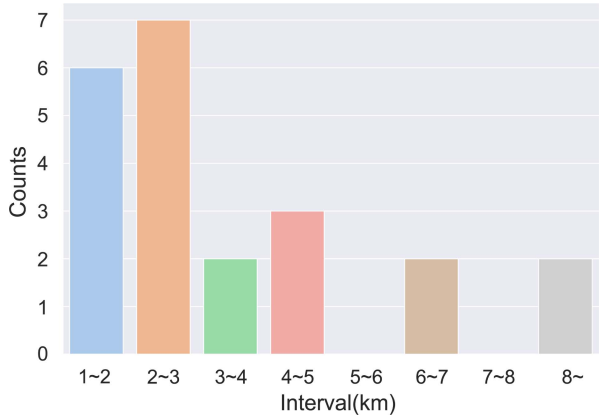

Fig. 8. Estimating the number distribution of radius in different intervals.

Furthermore, the dispersion of the MAE remains consistent as indicated by the standard deviation. Compared to the MAE, the MGD error distribution exhibits relatively greater dispersion. The standard deviation of MGD errors across all samples is 0.501 km. Analyzing the estimation errors by region revealed that the estimated cores in the Black Sea and East China Sea exhibit larger deviations from the labels ("truth").

A submesoscale eddy is a phenomenon with a diameter smaller than the Rossby radius of deformation, typically ranging from approximately 0.1 to 10 km horizontally and 0.01 to 1 km vertically. We calculated the radius distribution of the samples used in this study, as shown in Fig. 8, to analyze the radius information of these eddies captured by HiSea-II. The estimated radii in this study do not exceed 10 km, with most falling within 5 km. Although the number of samples is limited and the parameterization framework introduces some errors, the trend in radius distribution is consistent with that observed by the SDG satellite [69]. The number of eddies with radii within 3 km constitutes nearly half of the total which means the HiSea-II

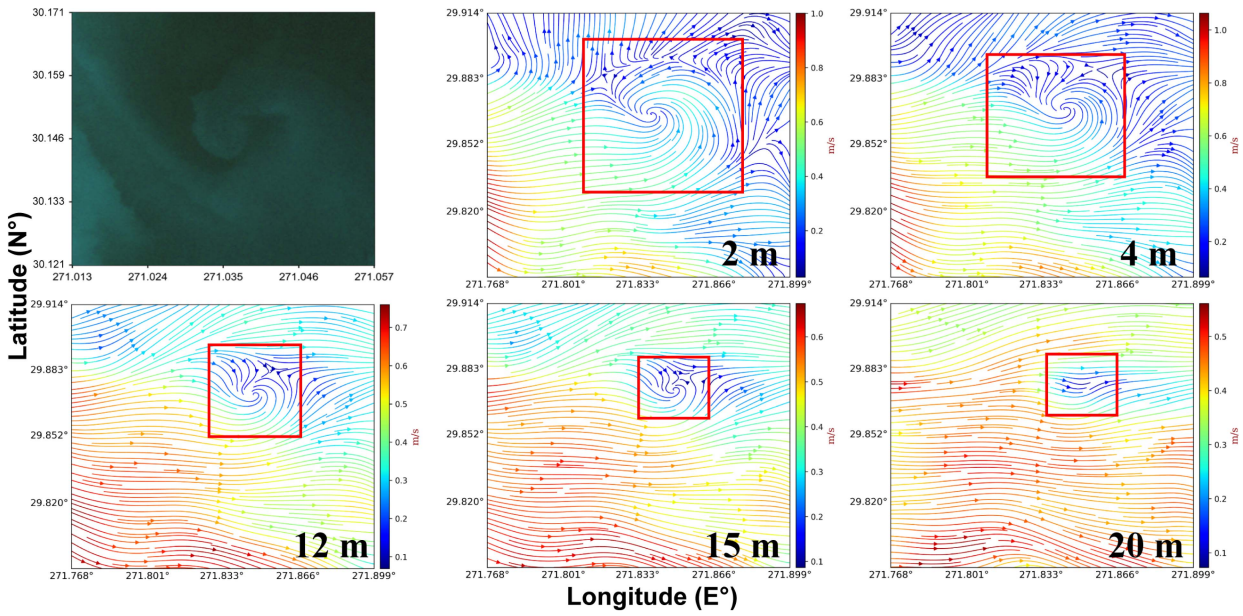

(a)

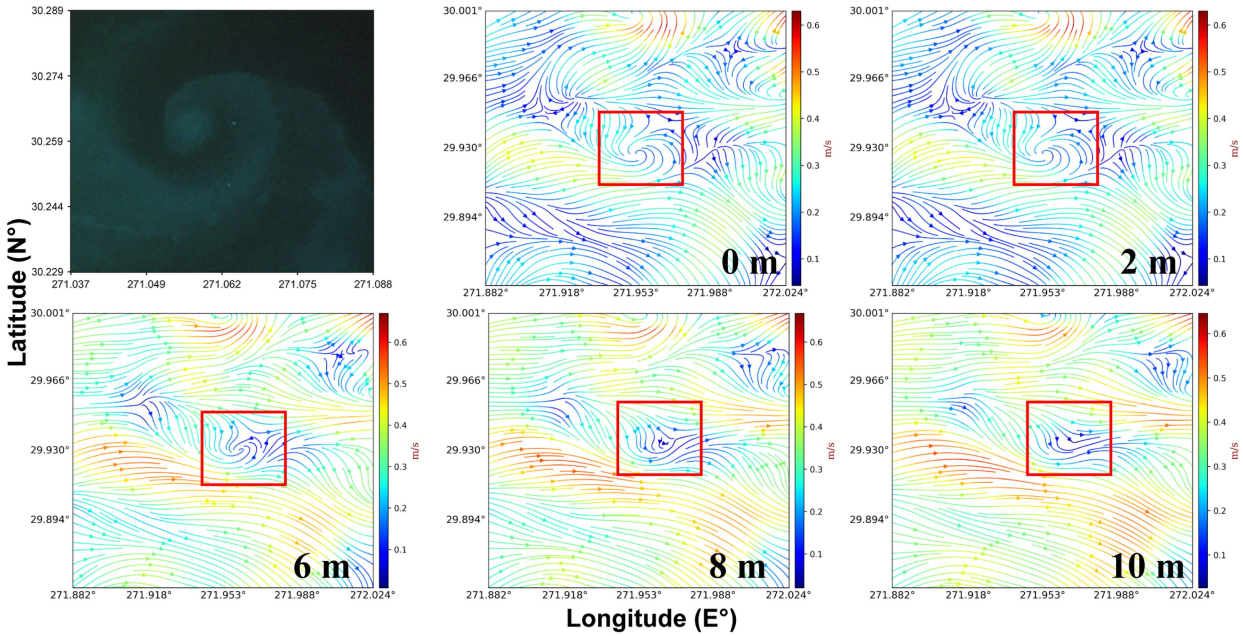

(b)

Fig. 9. Submesoscale images from the HiSea-II satellite in the Gulf of Mexico and matched current streamline of $1/100^{\circ}$ of the reanalysis ocean current at different depths. (a) Submesoscale eddy captured by the HiSea-II estimated depth of 14 m and below and to the right are current diagrams of different depths. (b) Submesoscale eddy captured by the HiSea-II estimated depth of 8 m and below and to the right are the same as (a).

captures a higher frequency of submesoscale eddies with radii around 3 km.

In addition to the horizontal parameters, such as core coordinates and radius, we estimated the vertical parameter, specifically the depth of the submesoscale eddies, using 3-D logarithmic spirals to depict their 3-D structures, as shown in Fig. 9. To verify the estimated vertical depths of the submesoscale eddies, we first queried the water depth data (ETOPO 2022) at the eddy locations, finding that all estimated depths were within the water depth range. We then matched the HyCOM-TSLS $1/100^{\circ}$ Gulf of Mexico reanalysis current data with the locations of the submesoscale eddies. Fig. 9 illustrates the ocean currents at various depths where the submesoscale eddies are located.

From Fig. 9, we can observe that the streamline images exhibit a shape analogous to the watercolor features observed in HiSea-II imagery. For eddy (a) in Fig. 9, it is evident that the size of this eddy diminishes with increasing depth, and the spiral structure dissipates at a depth of 20 m. It can be inferred that the depth of this submesoscale eddy lies between 15 and 20 m. The depth of this eddy, as estimated by our proposed framework, is 14 m, within its vertical structure. The depth of eddy (b) depicted in Fig. 9 is between 8 to 10 m, with our framework estimating it

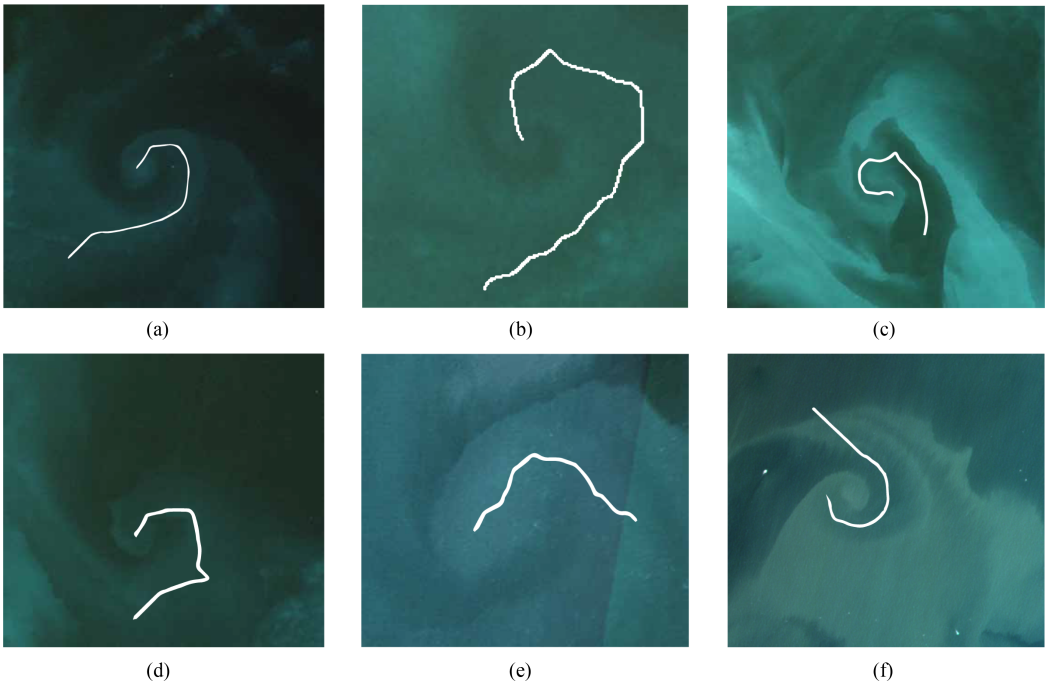

Fig. 10. Streamline of the submesoscale eddies processing with the Chan-Vese model. False-color is used to enhance the visualization of eddies.

TABLE II
ERROR OF PARAMETERIZED CORE LOCATION FOR CHAN-VESE METHOD AND NEURAL NETWORK

Channel	Number	MAE (°)	MGD (km)
Neural Network	10	0.006±0.005	0.885±0.684
Chan-Vese	11	0.004±0.003	0.691±0.439

at 8 m. To a certain extent, this current information validates the reasonableness of the depth parameters estimated by our proposed model.

In addition, information on the core, radius, and depth of the submesoscale eddy, and anticyclones or cyclones are particularly crucial for the study of eddy dynamics. However, the multispectral image displays an instantaneous watercolor state, which belongs to the static case without kinetic parameters. The identification of cyclonic and anticyclonic eddies is based on the outcomes of the spiral fit and the watercolor condition. From Fig. 7 and figures in supplementary material, the most intriguing finding is that most logarithmic spirals are counterclockwise, which suggests the submesoscale eddies studied here are cyclones. The reasons for this include the following: 1) Insufficient number of samples. These submesoscale eddies are located on the east coast of the mainland and are close to the coast, which has a sample bias. 2) The general situation. Most submesoscale eddies are cyclonic [63], [74], [75], [76].

C. Comparison of Branches

Relative to the neural network, the streamline of eddy extracted from the Chan-Vese channel is fitted to effectively determine the exact location of the eddy core. Further statistical tests are presented in Table II, revealed that the estimated results via the Chan-Vese channel have lower MAE and MGD. By fitting logarithmic spirals to the main streamlines, it is possible to achieve a more precise estimate of the eddy core and radius. To illustrate the streamline more visually, Fig. 10 displays the main streamlines of eddies extracted by the Chan-Vese model plotted on the multispectral image. From the figure, we can see that the streamlines can reflect the binding effect of eddies on the marine material and describe the rotation of eddies. This is because the Chan-Vese model belongs to the class of models based on region segmentation, which enables regions with different watercolor features to be effectively delimited. Under the action of an eddy, the material rotates and diffuses from the region of elevated concentration to the region of low concentration, which gives the region of elevated concentration the form of an eddy rotation, allowing the extraction of the main streamline. It can be observed that the streamlines in Fig. 10 begin at the center of the eddy, this guarantees the accuracy of delimiting the region of the core located.

D. Cross Verification With Multisource Data

To verify whether the submesoscale eddies detected from the multispectral images exhibit consistent dynamics with those shown in the Chl-a data, we need to find other optical satellites that can observe these regions at similar times. Therefore, we adopted the Chl-a concentration data from the GOCI-II and GCOM-C satellites. The spatial resolution of these data is 250 m, which is sufficient to observe submesoscale phenomena. In addition, the GOCI-II data has an hourly temporal resolution, while the GCOM-C can complete a global scan every two days. Consequently, the GOCI-II Chl-a data is suitable for verifying submesoscale eddies in the East China Sea, whereas eddies in the Black Sea and Gulf of Mexico can be verified using GCOM-C.

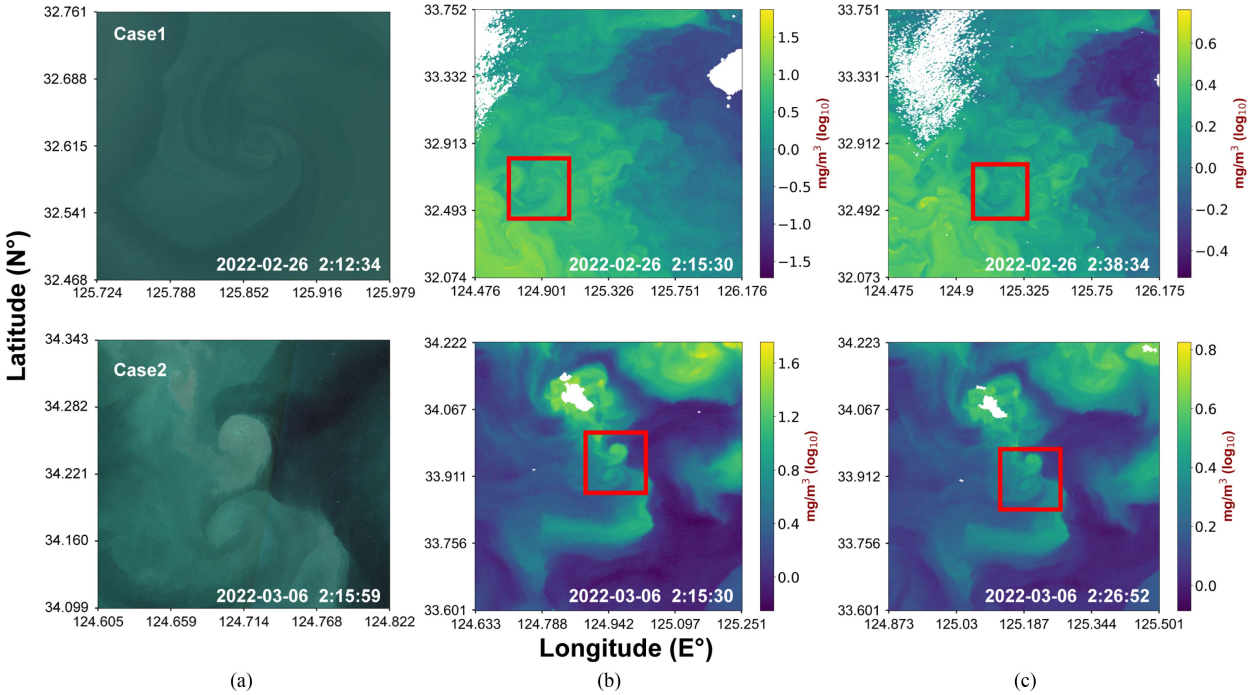

Fig. 11. Comparison between the watercolor features of submesoscale eddies in the East China Sea observed by HiSea-II and Chl-a data produced by GOCI-II. (a) and (c) Submesoscale eddies featured in HiSea-II imagery. (b) and (d) Chl-a data of GOCI-II. False-color is used to enhance the visualization of eddies.

The matching results for both GOCI-II and GCOM-C in the East China Sea are displayed in Fig. 11, and results for other regions are shown in the supplementary material.

By comparing the water color features captured by HiSea-II with the spiral characteristics of the Chl-a concentration from GOCI-II and GCOM-C, we observe that the Chl-a data displays a structure similar to the watercolor features in the HiSea-II images. In Case 1, as shown in Fig. 11, the eddy was observed to persist for at least 26 min. According to Fig. 11 and features in the supplementary material, other eddies are lived for at least 10 minutes.

We attempted to obtain continuous images from GOCI-II, but the optical satellite can be affected by cloud cover, making it challenging to observe an eddy continuously and without interruption. Nevertheless, these matching results demonstrate that we successfully verified the submesoscale eddies using high-resolution Chl-a concentration data, confirming that HiSea-II can observe submesoscale phenomena.

Beyond the proposed model's accuracy in estimating submesoscale eddy parameters, its computational efficiency is also crucial. We separately analyzed time consumption for different branches. The neural network requires an average of 12 min due to its iterative optimization of the eddy core position within the edge center region, with the lack of parallelization further extending runtime. In contrast, the Chan-Vese branch is significantly faster, completing the task in 47 s on average. This efficiency results from its segmentation and thinning process, which refines the extracted streamline to better resemble the eddy shape, reducing the number of iterations required to accurately compute the eddy core position and radius.

V. Conclusion

The proposed method efficiently tackles the issue of parameterizing submesoscale eddies. Different from traditional detection methods based on altimetry, our approach approximates the submesoscale morphology using a logarithmic spiral. We classify subimages into two categories based on watercolor characteristics and adopt model-driven and data-driven methods to achieve three-dimensional parameterization of a submesoscale eddy. The parameterized radius corresponds well to the horizontal extent of the submesoscale phenomenon. The experimental results indicate that the eddy core locations, as parameterized by our proposed framework, exhibit minimal errors. Furthermore, the parameterized submesoscale eddy radii and depths fall within reasonable ranges.

The generalizability of these results is subject to certain limitations. First, we manually labeled the region of interest for submesoscale eddies artificially, as opposed to training a network for automated recognition. This approach was necessitated by the scarcity of high-quality HiSea-II images with discernible submesoscale eddy water color features, which was insufficient to support model training. Consequently, this limitation has an impact on the overall generalization capability of our approach. Second, we approximate the problem of the submesoscale morphology as a logarithmic spiral. This spiral can be transformed into a linear form to simplify the problem. In future work, we need to explore functions that are better suited for the rotational structure of submesoscale eddies, providing a more precise description of their spiral patterns. Finally, it is important to note that the watercolor images used in this study are static state data. Therefore, our parameterization method focuses solely on estimating the depth,

core position, and radius of the submesoscale eddies. To achieve a more comprehensive understanding of submesoscale eddies, future studies could investigate the incorporation of additional parameters such as amplitude, energy, and velocity, while also addressing the aforementioned limitations, which would provide further insights into the dynamic nature of submesoscale eddies.

REFERENCES

[1] T. Du et al., "Growth of ocean thermal energy conversion resources under greenhouse warming regulated by oceanic eddies," *Nature Commun.*, vol. 13, no. 1, Nov. 2022, Art. no. 7249.

[2] S. Wang et al., "ElNiño/Southern oscillation inhibited by submesoscale ocean eddies," *Nature Geosci.*, vol. 15, no. 2, pp. 112–117, Feb. 2022.

[3] N. Beech, T. Rackow, T. Semmler, S. Danilov, Q. Wang, and T. Jung, "Long-term evolution of ocean eddy activity in a warming world," *Nature Climate Change*, vol. 12, no. 10, pp. 910–917, Oct. 2022.

[4] M. C. Arostegui, P. Gaube, P. A. Woodworth-Jefcoats, D. R. Kobayashi, and C. D. Braun, "Anticyclonic eddies aggregate pelagic predators in a subtropical gyre," *Nature*, vol. 609, no. 7927, pp. 535–540, Sep. 2022.

[5] G. Chen, J. Yang, and G. Han, "Eddy morphology: Egg-like shape, overall spinning, and oceanographic implications," *Remote Sens. Environ.*, vol. 257, May 2021, Art. no. 112348.

[6] J. Gula, J. Taylor, A. Shcherbina, and A. Mahadevan, "Chapter 8—submesoscale processes and mixing," in *Ocean Mixing*, M. Meredith and A. N. Garabato, Eds. New York, NY, USA: Elsevier, 2022, pp. 181–214.

[7] X. Capet, J. C. McWilliams, M. J. Molemaker, and A. F. Shchepetkin, "Mesoscale to submesoscale transition in the California current system. Part III: Energy balance and flux," *J. Phys. Oceanogr.*, vol. 38, no. 10, pp. 2256–2269, Oct. 2008.

[8] J. C. McWilliams, "Submesoscale currents in the ocean," *Proc. Roy. Soc. A: Mathematical, Phys. Eng. Sci.*, vol. 472, no. 2189, May 2016, Art. no. 20160117.

[9] R. Li, L. Xia, J. Yang, B. Huang, and G. Chen, "Towards submesoscale eddy detection in SDGSAT-1 data through deep learning," *Int. J. Digit. Earth*, vol. 17, no. 1, 2024, Art. no. 2369625.

[10] F. Kessouri, D. Bianchi, L. Renault, J. C. McWilliams, H. Frenzel, and C. A. Deutsch, "Submesoscale currents modulate the seasonal cycle of nutrients and productivity in the California current system," *Glob. Biogeochemical Cycles*, vol. 34, no. 10, Oct. 2020, Art. no. e2020GB006578.

[11] A. A. Kubryakov, O. S. Puzina, and A. I. Mizyuk, "Cross-slope buoyancy fluxes cause intense asymmetric generation of submesoscale eddies on the periphery of the black sea mesoscale anticyclones," *J. Geophys. Res.: Oceans*, vol. 127, no. 6, Jun. 2022, Art. no. e2021JC018189.

[12] P. Tedesco, J. Gula, C. Ménesguen, P. Penven, and M. Krug, "Generation of submesoscale frontal eddies in the Agulhas current," *J. Geophys. Res.: Oceans*, vol. 124, no. 11, pp. 7606–7625, 2019.

[13] F. Kessouri, D. Bianchi, L. Renault, J. C. McWilliams, H. Frenzel, and C. A. Deutsch, "Submesoscale currents modulate the seasonal cycle of nutrients and productivity in the California current system," *Glob. Biogeochemical Cycles*, vol. 34, no. 10, 2020, Art. no. e2020GB006578.

[14] X. Zhang, B. Huang, G. Chen, L. Ge, M. Radenkovic, and G. Hou, "Global oceanic mesoscale eddies trajectories prediction with knowledge-fused neural network," *IEEE Trans. Geosci. Remote Sens.*, vol. 62, 2024, Art. no. 4205214.

[15] X. Chen, G. Chen, L. Ge, C. Cao, and B. Huang, "Medium-range forecasting of oceanic eddy trajectory," *Int. J. Digit. Earth*, vol. 17, no. 1, 2024, Art. no. 2300325.

[16] G. Chen, X. Chen, and B. Huang, "Independent eddy identification with profiling argo as calibrated by altimetry," *J. Geophys. Research: Oceans*, vol. 126, no. 1, 2021, Art. no. e2020JC016729.

[17] X. Chen, G. Chen, L. Ge, B. Huang, and C. Cao, "Global oceanic eddy identification: A deep learning method from argo profiles and altimetry data," *Front. Mar. Sci.*, vol. 8, 2021, pp. 1–15.

[18] Y. Liu, H. Wang, F. Jiang, Y. Zhou, and X. Li, "Reconstructing 3-D thermohaline structures for mesoscale eddies using satellite observations and deep learning," *IEEE Trans. Geosci. Remote Sens.*, vol. 62, 2024, Art. no. 4203916.

[19] D. B. Chelton, M. G. Schlax, R. M. Samelson, and R. A. de Szoeke, "Global observations of large oceanic eddies: Global observations of oceanic eddies," *Geophys. Res. Lett.*, vol. 34, no. 15, Aug. 2007, Art. no. L15606.

[20] F. Tian, D. Wu, L. Yuan, and G. Chen, "Impacts of the efficiencies of identification and tracking algorithms on the statistical properties of global mesoscale eddies using merged altimeter data," *Int. J. Remote Sens.*, vol. 41, no. 8, pp. 2835–2860, Apr. 2020.

[21] A. Amores, G. Jordà, T. Arsouze, and J. Le Sommer, "Up to what extent can we characterize ocean eddies using present-day gridded altimetric products?," *J. Geophys. Res.: Oceans*, vol. 123, no. 10, pp. 7220–7236, 2018.

[22] D. Kang and E. N. Curchitser, "Gulf stream eddy characteristics in a high-resolution ocean model," *J. Geophys. Res.: Oceans*, vol. 118, no. 9, pp. 4474–4487, 2013.

[23] E. Mason, A. Pascual, P. Gaube, S. Ruiz, J. L. Pelegrí, and A. Delepoulle, "Subregional characterization of mesoscale eddies across the Brazil-Malvinas confluence," *J. Geophys. Res.: Oceans*, vol. 122, no. 4, pp. 3329–3357, 2017.

[24] Y. Zhang et al., "Bio-optical, physical, and chemical properties of a loop current eddy in the gulf of Mexico," *J. Geophys. Res.-Oceans*, vol. 128, no. 3, Mar. 2023, Art. no. e2022JC018726.

[25] D. L. Rudnick, G. Gopalakrishnan, and B. D. Cornuelle, "Cyclonic eddies in the gulf of Mexico: Observations by underwater gliders and simulations by numerical model," *J. Phys. Oceanogr.*, vol. 45, no. 1, pp. 313–326, Jan. 2015.

[26] G. Li, Y. He, G. Liu, Y. Zhang, C. Hu, and W. Perrie, "Multi-sensor observations of submesoscale eddies in coastal regions," *Remote Sens.*, vol. 12, no. 4, Feb. 2020, pp. 1–17.

[27] Y. Zhang, C. Hu, D. J. McGillicuddy Jr, Y. Liu, B. B. Barnes, and V. H. Kourafalou, "Mesoscale eddies in the gulf of Mexico: A three-dimensional characterization based on global HYCOM," *Deep-Sea Res. Part II-Topical Stud. Oceanogr.*, vol. 215, Jun. 2024, Art. no. 105380.

[28] S. Wang et al., "Weakened submesoscale eddies in the equatorial pacific under greenhouse warming," *Geophys. Res. Lett.*, vol. 49, no. 21, Nov. 2022, Art. no. e2022GL100533.

[29] S. Voisin et al., "Topological feature tracking for submesoscale eddies," *Geophys. Res. Lett.*, vol. 49, no. 20, Oct. 2022, Art. no. e2022GL099416.

[30] C. Dong et al., "Three-dimensional oceanic eddy analysis in the southern california bight from a numerical product," *J. Geophys. Res.-Oceans*, vol. 117, Jan. 2012, Art. no. C00H14.

[31] Z. Zhang and B. Qiu, "Surface chlorophyll enhancement in mesoscale eddies by submesoscale spiral bands," *Geophys. Res. Lett.*, vol. 47, no. 14, Jul. 2020, Art. no. e2020GL088820.

[32] X. Zhang, H. Dai, J. Zhao, and H. Yin, "Generation mechanism of an observed submesoscale eddy in the Chukchi Sea," *Deep Sea Res. Part I: Oceanographic Res. Papers*, vol. 148, pp. 80–87, Jun. 2019.

[33] Y. Zhang, C. Hu, Y. Liu, R. H. Weisberg, and V. H. Kourafalou, "Submesoscale and mesoscale eddies in the Florida Straits: Observations from satellite ocean color measurements," *Geophys. Res. Lett.*, vol. 46, no. 22, pp. 13262–13270, 2019.

[34] V. H. Kourafalou and H. Kang, "Florida current meandering and evolution of cyclonic eddies along the Florida keys reef tract: Are they interconnected?," *J. Geophys. Res.: Oceans*, vol. 117, no. C5, 2012, Art. no. C05028.

[35] P. A. Ernst, B. Subrahmanyam, C. B. Trott, and A. Chaigneau, "Characteristics of submesoscale eddy structures within mesoscale eddies in the gulf of Mexico from 1/48 ECCO estimates," *Front. Mar. Sci.*, vol. 10, 2023, pp. 1–18.

[36] F. M. Bingham et al., "Simulated sea surface salinity data from a 1/48 ocean model," *Sci. Data*, vol. 11, no. 1, May 2024, Art. no. 532.

[37] G. Li et al., "The characteristics of submesoscale eddies near the coastal regions of eastern Japan: Insights from sentinel-1 imagery," *J. Mar. Sci. Eng.*, vol. 12, no. 5, 2024, Art. no. 761.

[38] A. Aleskerova et al., "Characteristics of topographic submesoscale eddies off the crimea coast from high-resolution satellite optical measurements," *Ocean Dyn.*, vol. 71, no. 6/7, pp. 655–677, Jul. 2021.

[39] C. Huang, L. Zeng, D. Wang, Q. Wang, P. Wang, and T. Zu, "Submesoscale eddies in eastern Guangdong identified using high-frequency radar observations," *Deep Sea Res. Part II: Topical Stud. Oceanogr.*, vol. 207, Feb. 2023, Art. no. 105220.

[40] L. Xia, B. Huang, R. Li, and G. Chen, "A two-stage deep learning architecture for detection global coastal and offshore submesoscale ocean eddy using SDGSAT-1 multispectral imagery," *Sci. Remote Sens.*, vol. 10, 2024, Art. no. 100174.

[41] R. Nian et al., "Different types of surface chlorophyll patterns of oceanic mesoscale eddies identified by AI framework," *J. Geophys. Res.: Oceans*, vol. 129, no. 9, 2024, Art. no. e2024JC021176.

[42] H. Gao, B. Huang, G. Chen, L. Xia, and M. Radenkovic, "Deep learning solver unites SDGSAT-1 observations and Navier–Stokes theory for oceanic vortex streets," *Remote Sens. Environ.*, vol. 315, 2024, Art. no. 114425.
[43] Z. Lee et al., "SmallSat for monitoring aquatic ecosystem of coastal and inland waters: The experience of HiSea-II," *IEEE Trans. Geosci. Remote Sens.*, vol. 62, 2024, Art. no. 1002010.
[44] Y. Wang, J. Yang, K. Wu, M. Hou, and G. Chen, "A submesoscale eddy identification dataset derived from GOCI I chlorophyll–a data based on deep learning," *Earth Syst. Sci. Data Discuss.*, vol. 2023, pp. 1–23, 2023.
[45] L. Xia, G. Chen, X. Chen, L. Ge, and B. Huang, "Submesoscale oceanic eddy detection in SAR images using context and edge association network," *Front. Mar. Sci.*, vol. 9, 2022, pp. 1–16.
[46] E. Khachatrian, N. Sandalyuk, and P. Lozou, "Eddy detection in the marginal ice zone with sentinel-1 data using YOLOv5," *Remote Sens.*, vol. 15, no. 9, 2023, Art. no. 2244.
[47] C. E. Buckingham et al., "Testing Munk's hypothesis for submesoscale eddy generation using observations in the North Atlantic," *J. Geophys. Res.: Oceans*, vol. 122, no. 8, pp. 6725–6745, 2017.
[48] Z. Zhang et al., "Submesoscale eddies detected by SWOT and moored observations in the Northwestern Pacific," *Geophys. Res. Lett.*, vol. 51, no. 15, 2024, Art. no. e2024GL110000.
[49] O. Ronneberger, P. Fischer, and T. Brox, "U-Net: Convolutional networks for biomedical image segmentation," in *Medical Image Computing and Computer-Assisted Intervention–MICCAI 2015*, vol. 9351. Cham, Switzerland: Springer International Publishing, 2015, pp. 234–241.
[50] H. Wang and X. Li, "DeepBlue: Advanced convolutional neural network applications for ocean remote sensing," *IEEE Geosci. Remote Sens. Mag.*, vol. 12, no. 1, pp. 138–161, Mar. 2024.
[51] M. Pu, Y. Huang, Y. Liu, Q. Guan, and H. Ling, "EDTER: Edge detection with transformer," in *Proc. IEEE/CVF Conf. Comput. Vis. Pattern Recognit.*, Jun. 2022, pp. 1402–1412.
[52] Y. LeCun, Y. Bengio, and G. Hinton, "Deep learning," *Nature*, vol. 521, no. 7553, pp. 436–444, May 2015.
[53] B. Huang, L. Ge, X. Chen, and G. Chen, "Vertical structure-based classification of oceanic eddy using 3-D convolutional neural network," *IEEE Trans. Geosci. Remote Sens.*, vol. 60, 2022, Art. no. 4203614.
[54] X. Chen, G. Chen, L. Ge, B. Huang, and C. Cao, "Global oceanic eddy identification: A deep learning method from Argo profiles and altimetry data," *Front. Mar. Sci.*, vol. 8, May 2021, Art. no. 646926.
[55] Y. Liu and X. Li, "Impact of surface and subsurface-intensified eddies on sea surface temperature and chlorophyll a in the Northern Indian ocean utilizing deep learning," *Ocean Sci.*, vol. 19, no. 6, pp. 1579–1593, 2023.
[56] X. Meng, Y. Bao, Y. Wang, X. Zhang, and H. Liu, "An advanced soil organic carbon content prediction model via fused temporal-spatial-spectral (TSS) information based on machine learning and deep learning algorithms," *Remote Sens. Environ.*, vol. 280, Oct. 2022, Art. no. 113166.
[57] X. Li et al., "Deep-learning-based information mining from ocean remote-sensing imagery," *Nat. Sci. Rev.*, vol. 7, no. 10, pp. 1584–1605, Mar. 2020.
[58] Z. Ban, X. Hu, and J. Li, "Tipping points of marine phytoplankton to multiple environmental stressors," *Nature Climate Change*, vol. 12, no. 11, pp. 1045–1051, Nov. 2022.
[59] G. Zheng, X. Li, R.-H. Zhang, and B. Liu, "Purely satellite data–driven deep learning forecast of complicated tropical instability waves," *Sci. Adv.*, vol. 6, no. 29, 2020, Art. no. eaba1482.
[60] T. Chan and L. Vese, "Active contours without edges," *IEEE Trans. Image Process.*, vol. 10, no. 2, pp. 266–277, Feb. 2001.
[61] B. Huang et al., "Nonlocal graph theory based transductive learning for hyperspectral image classification," *Pattern Recognit.*, vol. 116, Aug. 2021, Art. no. 107967.
[62] C. Pegliasco, A. Delepoulle, E. Mason, R. Morrow, Y. Faugère, and G. Dibarboure, "META3.1exp: A new global mesoscale eddy trajectory atlas derived from altimetry," *Earth Syst. Sci. Data*, vol. 14, no. 3, pp. 1087–1107, 2022.
[63] W. Munk, L. Armi, K. Fischer, and F. Zachariasen, "Spirals on the sea," in *Proc. Roy. Soc. London. Ser. A: Mathematical, Phys. Eng. Sci.*, vol. 456, no. 1997, pp. 1217–1280, 2000.
[64] NOAA National Centers for Environmental Information, "Etopo 2022 15 arc-second global relief model," 2022, doi: 10.25921/FD45-GT74.
[65] M. Everingham, L. Van Gool, C. K. I. Williams, J. Winn, and A. Zisserman, "The PASCAL visual object classes challenge 2012 (VOC2012) results," 2012, [Online]. Available: https://www.bibsonomy.org/bibtex/2af3e05b5f98957bd59f03f37fad407c5/tgandor
[66] P. Arbeláez, M. Maire, C. Fowlkes, and J. Malik, "Contour detection and hierarchical image segmentation," *IEEE Trans. Pattern Anal. Mach. Intell.*, vol. 33, no. 5, pp. 898–916, May 2011.
[67] O. Ronneberger, P. Fischer, and T. Brox, "U-net: Convolutional networks for biomedical image segmentation," in *Medical Image Computing and Computer-Assisted Intervention–MICCAI 2015*, N. Navab, J. Hornegger, W. M. Wells, and A. F. Frangi, Eds. Cham, Switzerland: Springer International Publishing, 2015, pp. 234–241.
[68] Y. Liu et al., "Richer convolutional features for edge detection," *IEEE Trans. Pattern Anal. Mach. Intell.*, vol. 41, no. 8, pp. 1939–1946, Aug. 2019.
[69] R. Liu, W. Pu, H. Nan, and Y. Zou, "Retina image segmentation using the three-path Unet model," *Sci. Rep.*, vol. 13, no. 1, Dec. 2023, Art. no. 22579.
[70] M. Yang, Y. Yuan, and G. Liu, "SDUNet: Road extraction via spatial enhanced and densely connected Unet," *Pattern Recognit.*, vol. 126, 2022, Art. no. 108549.
[71] T. Y. Zhang and C. Y. Suen, "A fast parallel algorithm for thinning digital patterns," *Commun. ACM*, vol. 27, no. 3, pp. 236–239, Mar. 1984.
[72] M. A. Fischler and R. C. Bolles, "Random sample consensus: A paradigm for model fitting with applications to image analysis and automated cartography," *Commun. ACM*, vol. 24, no. 6, pp. 381–395, Jun. 1981.
[73] D. P. Kingma and J. Ba, "Adam: A method for stochastic optimization," in *Proc. Int. Conf. Learn. Representations*, 2015, pp. 1–15.
[74] L. N. Thomas, A. Tandon, and A. Mahadevan, *Submesoscale Processes and Dynamics* (Geophysical Monograph), vol. 177. Washington, DC, USA: American Geophysical Union, 2008, pp. 17–38.
[75] A. Kubryakov, A. Aleskerova, E. Plotnikov, A. Mizyuk, A. Medvedeva, and S. Stanichny, "Accumulation and cross-shelf transport of coastal waters by submesoscale cyclones in the black sea," *Remote Sens.*, vol. 15, no. 18, 2023, Art. no. 4386.
[76] A. V. Zimin, O. A. Atazhanova, D. A. Romanenkov, I. E. Kozlov, and B. Chapron, "Submesoscale eddies in the white sea based on satellite radar measurements," *Izvestiya, Atmos. Ocean. Phys.*, vol. 57, no. 12, pp. 1705–1711, 2021.